Electronic Supplementary Material (ESI) for Journal of Materials Chemistry A.

Electronic Supplementary Information (ESI) for

In-situ crystal engineering on digital light processing (DLP) 3D-printed woodpile scaffolds: A monolith catalyst with highly accessible active sites for enhanced catalytic cracking

Ruoyu Wang[1], Yixuan Gong[1], Peng Wang[1], Wenhui He[1], Ye Song[1], Mudi Xin[1], Qiuqiao Jiang[1], Yuchen Sha[1], Tiantian Cao[2], Haitao Song[1], and Wei Lin[1*]

[1] Research Institute of Petroleum Processing, SINOPEC, Beijing 100083, China.
[2] China Petrochemical Corporation (SINOPEC Group), Beijing, China.

*Corresponding author. Email: linwei.ripp@sinopec.com

This PDF file includes a total of 39 pages.

Content

1 Materials and Methods

1.1 Materials

Diatomite and metakaolin powders were supplied by Lingshou Mineral Products Processing Factory, China. Phenylbis (2, 4, 6-trimethylbenzoyl) phosphine oxide, polyethylene glycol (600) dimethacrylate (PEG600DMA), poly(ethylene glycol) (400) (PEG400), and tripropylene glycol diacrylate (TPGDA) were purchased from Aldrich-Sigma. Aluminium sulfate, sodium hydroxide and tetrapropyl-ammoniuhydroxide (TPAOH, 25wt% aq.), poly dimethyl diallyl ammonium chloride (PDDA, 20 wt% aq.), 1,3,5-triisopropylbenzene (TIPB) and *n*-octane were obtained from Innochem Co., Ltd. Silica sol (Ludox AS40) was purchased from Grace Company. Conventional microporous ZSM-5 powder (C-ZSM-5, H-type) with a SAR (Si to Al molar ratio) of 18 was obtained from SINOPEC catalyst Co., Ltd.

1.2 Methods

1.2.1 Ink preparation and DLP 3D printing

The 3D printing ink for woodpile scaffolds fabrication was prepared through mixing photosensitive resin and raw powders of aluminosilicate minerals. Briefly, the photosensitive resin was prepared by mixing 35 wt% of TPGDA, 30 wt% PEG600DMA, 30 wt % PEG400 and 5 wt % of phenylbis (2, 4, 6-trimethylbenzoyl) phosphine oxide. The as-prepared photosensitive resin was treated with ultrasonic for 30 min at room temperature. Then 78 g of kaolin (dry basis) and 52 g of diatomite (dry basis) were added into 200 g of the photosensitive resin under stirring, and the obtained mixture was milled using a three-roll planetary mill for three times at room temperature to obtain the photosensitive ink for 3D printing. See **Figure S1** and **Table S2** for the morphologies and the particle size distributions of two aluminosilicate mineral powders, respectively.

The designed three-dimensional model (STL format) was sliced and printed by a DLP 3D printer (SU-100A, CeraEPI, China) using the prepared ink under UV light (405 nm). The photograph of the DLP 3D printer used in this work and its structural diagram are shown in **Figure S2**. During DLP printing, the optical power density is controlled at 1 mW/cm^2. The cured green body was throughly washed using deionized (DI) water, and was cleaned by ultrasonic in 50 vol% ethanol aqueous solution to remove adherent ink slurries. The cleaned green body is sintered in a furnace following the designed process (**Figure S3**) to obtain the final WP scaffold.

1.2.2 Fabrication of the monolith catalyst (MC-Z)

Preparation of the crystal seed (CS) and CS-WP composite. The synthesis solution of ZSM-5 crystal seed was prepared by dissolving aluminium sulfate into sodium hydroxide solution, and then adding silica sol. The obtained mixture was stirred for 4 h at room temperature and then a certain amount of TPAOH solution was added. After being stirred at room temperature for 18 h, the resultant mixture (molar composition: $11.9Na_2O : Al_2O_3 : 89.6SiO_2 : 9.9TPAOH : 3800H_2O$) was loaded into an autoclave for hydrothermal treatment at 170 °C for 16 h. The as-synthesized solid product was used as the crystal seeds (CS). To prepare CS-WP composite, the WP scaffold was immersed into 100 mL of 0.2 wt% PDDA aqueous solution under constant stirring. After being stirred for 2 h, the WP scaffold was collected from the solution, and was washed with DI water. Then 0.3 g of the as-prepared CS particles and the PDDA-treated WP scaffold were added into 100 mL of water. After being stirred for 2 h at room temperature, the scaffold was collected from the mixture and was dried at 120 °C, then it was calcinated at 550 °C for 4 h to obtain crystal seed adsorbed WP (CS-WP) scaffold.

In-situ crystallization of ZSM-5 on CS-WP scaffold. The synthesis solution was prepared by dissolving aluminium sulfate into sodium hydroxide solution, and then adding silica sol and TPAOH. After being stirred at room temperature for 4 h, the resultant mixture (molar composition: 11.9Na_2O : Al_2O_3 : 89.6SiO_2 : 9.9TPAOH : 3800H_2O) was loaded into an autoclave for hydrothermal treatment at 170 ºC for 6 h. Then the CS-WP scaffold was put into the obtained solution in autoclave for another 24 h of hydrothermal treatment at 170 °C. After the synthesis, the scaffold was taken out, thoroughly washed with DI water and dried at 120 ºC for 4 h. Then the scaffold was calcinated at 550 °C for 4 h to remove the residual template molecules, and the obtained scaffold was investigated as the monolith catalyst (MC-Z).

Two reference catalysts (C-Cat-1 and C-Cat-2) were used in this work. C-Cat-1 was a monolith zeolitic catalyst fabricated using the same method as that of MC-Z, except that C-Cat-1 has conventional straight channels rather than interconnected ones (**Figure S9**). C-Cat-2 was a granulated catalyst (20–40 mesh particles) composed of inert fumed silica and C-ZSM-5 zeolite powder that has a similar SAR to that of ZSM-5 crystals *in-situ* crystallized on the surface of MC-Z (**Figure S10**). The two reference catalysts have similar degrees of crystallinities and the zeolite components therein have approximate SAR values (**Tables S6-S8**).

1.2.3 Catalytic tests

Before the catalytic cracking reaction, the fabricated Na-type catalysts were immersed in 1 M $(NH_4)_2SO_4$ aqueous solution under stirring for 2 h at 80 °C. This ion-exchange process was repeated for two times. Thereafter, the NH_4-type catalysts were washed, dried, and calcinated at 550 °C for 4 h. The obtained H-type samples were used as catalysts in cracking reactions.

Catalytic cracking of *n*-octane/TIPB. The cracking reactions of TIPB and *n*-octane over different catalysts were performed in a fixed-bed continuous-flow reactor. In a typical run, the catalysts were put in the flat-temperature zone of the reactor tube. The reactant

(TIPB) was mixed with N_2 carrier gas via a ram pump, and the feeding time for TIPB is 600 s with a flow rate of 0.071 g/min. The catalytic reactions were conducted at 450 °C and 550 °C with a catalyst to oil mass ratio of 2.5. For the cracking reactions of *n*-octane over different catalysts, the reactant (*n*-octane) was mixed with N_2 carrier gas via a ram pump, providing different reaction WHSVs (65, 91 and 151 h^{-1}). The catalytic reactions were conducted at 675 ºC or 500 ºC with different catalyst to oil mass ratios. After reaction, the liquid products were collected in a glass receiver kept in an ice bath, and the gaseous products were collected in a burette by water displacement. The liquid products were detected by an Agilent 7890B GC equipped with a HP-PONA column (19091s-001) for composition analysis. The gas components were quantitatively analyzed by an Agilent 6890 GC equipped with ChemStation software.

The conversion of TIPB/*n*-octane, and the yield and selectivity of products were calculated according to the following equations:

$$\text{conversion} = \frac{m_0 - m_\text{p}}{m_0} \times 100\%$$

$$\text{yield}_\text{i} = \frac{m_\text{i}}{m_0} \times 100\%$$

$$\text{selectivity}_\text{i} = \frac{\text{yield}_\text{i}}{\text{conversion}} \times 100\%$$

where m_0 is reactant (TIPB/*n*-octane) feed mass, m_p is reactant mass in the product, m_i is mass of a particular component (*i*).

Thermal cracking of n-octane. The experimental procedure is the same as described for the catalytic reaction, except that the reactor is not loaded with catalyst but the quartz bead (20-40 mesh particles) instead.

1.2.4 CFD simulation

The effect of monolith structure on flow regime, mainly on fluid dynamics, is investigated using COMSOL Multiphysics. The flow is considered laminar due to its low Reynolds Number. The boundary conditions are set as follows: inlet volumetric flow rate =33.91 mL/min (corresponding to WHSV = 151 h^{-1}), temperature = 675 °C, outlet gauge pressure = 0 Pa,. The physical properties of mixed gas are set as follows: inlet gas density = 1.48 $kg \cdot m^{-3}$, gas kinetic viscosity = 1.72×10^{-5} Pa·s.[1]) Both boundary conditions and physical properties of inlet gases are consistent with that of the actual experiment.

1.2.5 Characterizations

Atomic force microscopes (AFM). AFM measurements (tapping mode) were carried out on a Cyper ES (Asylum Research) using an AC200TS -R3 (Olympus) cantilever with a spring constant of 9 nN/nm. Scan speed: 2.44 Hz; Probe frequency: 150 kHz.

Brunauer–Emmett–Teller (BET) characterization. BET surface areas were calculated by the Brunauer-Emmett-Teller (BET) method from the N_2 desorption data. The contributions from both micro- and mesoporosity were calculated using the t-plot and the Barrett-Joyner-Halenda (BJH) model.

Electron probe microanalysis (EPMA). EPMA was measured by a electron probe microanalyzer (JEOL Ltd., JXA-8530F PLUS).

Hg intrusion. The porosity from meso- to macropores was examined by Hg-porosimetry using an Autopore 9520 (Micromeritics, Mönchengladbach, Germany).

Inductively coupled plasma (ICP) analysis. The concentrations of Si and Al in filtrates were analyzed by an inductively coupled plasma spectrometer (5110 ICP, Agilent Technologies).

Ion beam polishing. Argon ion beam polishing was conducted using an Argon ion polisher (Fischione Ltd., SEM Mill).

Magic angle spinning nuclear magnetic resonance (MAS NMR) spectroscopy. The solid-state MAS NMR analyses of the samples were performed on a Bruker AVANCE III 600WB spectrometer equipped with a 4 mm triple resonance MAS probe and 7 mm double resonance MAS probe for ^{27}Al and ^{29}Si, respectively. The spinning rates were 5 kHz and 12 kHz corresponding to ^{29}Si and^{27}Al MAS NMR, respectively. The ^{27}Al MAS NMR spectra were obtained using 0.4 μs ($< \pi/15$) pluses at a resonance frequency field of 156.4 MHz and a recycle delay of 1 s. The ^{29}Si MAS NMR spectra were obtained using 1.8 μs pluses at a resonance frequency field of 99.3 MHz.

Mechanical testing. Mechanical testing was carried out using a mechanical testing device (CMT6103, MTS, China). The monolithic catalyst was placed between two metal plates and compressed with a 500 N load cell at 2 mm/min. The compressive force was applied in the axial direction until the monoliths broke.

NH_3-TPD. The acidic properties of the catalysts were analyzed by temperature-programed desorption of ammonia (NH_3-TPD) on a Micromeritics Auto chem II 2920 apparatus equipped with a thermal conductivity detector (TCD) unit.

Particle size determination. The particle size distribution of the microspheres was determined using a Mastersizer 2000 (Malvern Instruments, Worcestershire, UK). The angular intensity of the scattered light was measured using a series of photosensitive detectors in Mastersizer 2000. The particle size distribution was determined based on Mie scattering theory. In each test, samples were diluted in DI-water to avoid multiple scattering. The size distribution of each sample was measured at least five times. The recorded average sizes are volume-averaged diameters.

Pyridine-adsorbed IR (Py-IR). Py-IR spectroscopy was measured by a Nicolet Magna-IR 560 ESP spectrophotometer (USA) with a resolution of 1 cm^{-1}. The sample to be measured was finely ground and pressed into a self-supporting wafer. The wafer was dehydrated in the IR cell at 500 ºC for 5 h under vacuum. After the temperature was decreased to room temperature, the adsorption of purified pyridine vapor followed for 20 min. Then the system was evacuated at 200 ºC or 350 ºC, and the spectra were recorded. The amount of the probe molecules (pyridine) adsorbed was determined by using the integrated area of a given band with the reported molar extinction coefficient.[1]

Rheological characterizations. The rheological measurements of the liquid resin and the aluminosilicate-based ink slurry were conducted on a HAAKE MARS 60 rheometer (Thermo Haake, Germany) equipped with an 8 mm disposable glass rotor. The time sweep measurement of the storage modulus (G') and loss modulus (G'') were performed under ultraviolet light (Omnic S2000, 320-500 nm, 5 mw/cm^2), and the thickness of the radiation sample was 0.1 mm. Each oscillation time scanning (5 Hz) lasted for 300s, and UV radiation was turned on at 120s lasted for 60s.

Scanning electron microscopy (SEM). A Hitachi S4800 electron microscope was used to investigate the crystal size and morphology of the aluminosilicate samples.

Scanning transmission electron microscopy (STEM). STEM images were obtained by using a JEM-ARM200F microscope (JEOL, Japan). The elemental distribution of the materials were determined by STEM mapping.

Thermal analysis. The thermogravimetric (TGA) and differential scanning calorimetric (DSC) curves were measured using a thermal analyzer (NETZSCH STA 449F3) with a alumina crucible. The analyses were performed with an air flow rate of 100 ml/min and a heating rate of 10 ºC/min from room temperature to 1100 ºC.

X-ray photoelectron spectroscopy (XPS). XPS characterization was performed on a Thermo Scientific K-Alpha instrument with a beam size of 400 μm.

X-ray diffraction (XRD). X-ray diffraction (XRD) patterns (2θ ranging from 5° to 70°) were measured by an Empyrean X-ray diffractometer (PANalytical Corporation, Netherland) using Cu K_{α} radiation (tube current 40 mA, voltage 40 kV). The relative crystallinities were calculated by the integral areas of peaks from 22.5° to 25.0° using a standard Y zeolite sample as the reference.

X-ray micro-computed tomography (μ-CT). The μ-CT images were acquired using a Bruker microCT system (SkyScan 2211). The X-ray focal spot size (Nominal) used was 35 μm and the energy used was 50 kV, working at 370 μA. The exposure time was 700 ms. The image pixel size was 0.20 μm. Image reconstruction was performed using NRecon Server (Version 1.7.3.0; Bruker Inc., Billerica, MA) and CT-Analyser (Version 1.13; Bruker Inc., Billerica, MA).

X-ray fluorescence (XRF). XRF spectroscopy was used to elemental contents of different samples on a ZSX Primus II (Rigaku) apparatus.

Zeta potential. Surface charge properties were determined by zeta potentials on a Malvern Zetasizer Nano ZS90 instrument.

2 Supplementary Movies

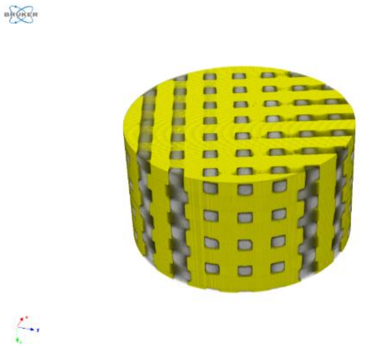

Filename: Movie S1.mp4

Raw tomographic slices series of the cured green body

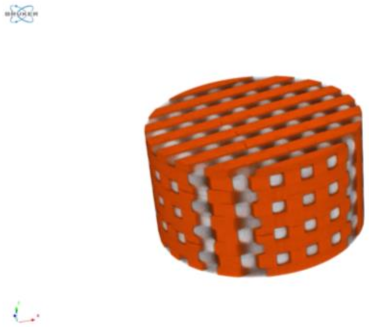

Filename: Movie S2.mp4

Raw tomographic slices series of the WP sample

3 Supplementary Tables

Table S1. 3D-printed monolithic catalysts by post-functionalization

No.	3D printing technique	Post-functionalization method	Active component	Loading (wt%)	Ref.
1	direct ink writing (DIW)	recrystallization	SAPO-34	4.9	[2]
2	direct ink writing (DIW)	recrystallization	SAPO-34	11.2	[2]
3	digital light processing (DLP) (printed template)	recrystallization	ZSM-5	9~19	[3]
4	Stereolithography	dip coating	CuO/CeO_2	3~9	[4]
5	direct metal laser sintering (DMLS) technique	impregnation	Pt nanoparticles	0.12	[5]
6	direct ink writing (DIW)	impregnation	Cr, Cu, Ni, and Y metal precursors	10	[6]

Table S2. Particle size distributions of the aluminosilicate powders

Size[a]/μm	metakaolin	diatomite
0~20	0.0	3.9
0~40	3.9	14.5
0~80	57.4	59.9
0~105	82.4	79.4
0~149	98.1	95.1
D90 [b]	118.3	128.6
APS [c]	74.6	70.6

[a] The recorded sizes are volume-averaged diameters.

[b] D90 = the particle size corresponding to 90% cumulative distribution of a sample.

[c] APS = average particle size.

Table S3. Fitting results of power-law fluids (η = mγ^{n-1})

Sample	m	n	R^2
Resin	91.22	0.08	0.991
3D printing ink	635.68	0.46	0.997

Table S4. Porosity analysis of two monoliths based on μ-CT results

Item	Cured green body	Sintered WP scaffold
Bone volume (μm^3)	8.86×10^{11}	5.29×10^{11}
Tissue volume (μm^3)	1.44×10^{12}	8.47×10^{11}
Bone surface (μm^2)	2.88×10^{9}	2.18×10^{9}
Tissue surface (μm^2)	7.57×10^{8}	5.33×10^{8}
Total porosity (%)	38.6	37.6

Note: The image reconstruction and data processing were performed using NRecon Server (Version 1.7.3.0; Bruker Inc., Billerica, MA) and CT-Analyser (Version 1.13; Bruker Inc., Billerica, MA).

Table S5. Zeta potentials of the crystal seed and scaffolds used in this work

Sample	Average Zeta potential/ mV[a]
CS	–23.6
WP	–13.5
PDDA-WP	20.4
CS-WP	–3.9

[a] The average result of three measurements

Table S6. Chemical compositions of the minerals and catalysts

Component (wt%)	Al_2O_3	SiO_2	Na_2O	SAR[a]
metakaolin	47.1	49.8	0.2	0.9
diatomite	2.8	95.1	0.3	28.6
CS	8.32	86.2	4.9	8.7
WP	28.8	66.7	0.4	1.9
MC-Z (bulk)	25.9	62.4	0.3	2.0
C-Cat-1 (bulk)	28.1	66.7	0.2	2.0
C-ZSM-5	4.5	95.2	0.07	18.0

[a] The silicon to aluminium molar ratio (SAR) in this table refers to the molar ratio of Si and Al, which is calculated according to the XRF results.

Table S7. Textual properties of the minerals and catalysts

Sample	S_{BET}[a] (m^2/g)	S_{micro}[b] (m^2/g)	S_{meso}[c] (m^2/g)	V_{total}[d] (cm^3/g)	V_{micro}[b] (cm^3/g)	V_{meso}[e] (cm^3/g)
WP	4	<1	4	0.008	<0.001	0.008
CS	6	2	4	0.009	<0.001	0.009
CS-WP	4	2	2	0.006	<0.001	0.006
MC-Z	219	183	36	0.128	0.072	0.056
C-Cat-1	238	201	37	0.150	0.080	0.070
C-ZSM-5	361	289	72	0.167	0.116	0.051

[a] Brunauer-Emmett-Teller (BET) method.

[b] *t*-plot method.

[c] S_{BET}-$S_{\mathrm{micro.}}$

[d] Volume of N_2 adsorbed at $P/P_0 = 0.99$.

[e] V_{total}-V_{micro}.

Table S8. Acidity properties of SCD-Y and C-Cat determined by Py-IR

Sample	Amout of acid sites (μmol/g)			
	200 ºC		350 ºC	
	B	L	B	L
MC-Z	47.2	56.1	23.9	22.8
C-Cat-1	48.4	44.1	29.6	21.1
C-Cat-2	50.8	29.7	26.5	7.4

Table S9. Yields of C_1, C_2, i-C_4^0 products and the cracking mechanism ratios (CMRs) of different catalysts

Yield or CMR	MC-Z	C-Cat-1	C-Cat-2
C_1, wt%	0.66%	0.23%	0.31%
C_2, wt%	2.14%	0.88%	1.24%
$C_2^=$, wt%	2.88%	1.91%	1.99%
i-C_4^0, wt%	4.64%	2.19%	2.66%
CMR	2.7	3.0	2.9

Note: CMR = $(C_l + \sum C_2)/i\text{-}C_4^0$, where C_1, $\sum C_2$, and i-C_4^0 denote the molar selectivities to methane, total C_2 hydrocarbons, and iso-butane, respectively.

Table S10. Catalytic performances of the monolith catalyst and some state-of-the-art zeolite catalysts

No.	Reactant	Reaction conditions	Catalyst	Conversion	Ref.
1	TIPB	450 ℃ TOS = 600 s	monolith ($^1RC_{ZSM\text{-}5}$ = 41.2%)	53%	this work
2	TIPB	400 ℃ TOS = 600 s	particles hierarchical ZSM-5	2~36%	[7]
3	TIPB	400 ℃ TOS = 300 min	particles plate-like ZSM-5	65%	[8]
4	TIPB	400 ℃ TOS = 8 h	particles caterpillar-shaped hierarchical ZSM-5	75%	[9]
5	TIPB	400 ℃ TOS = 8 h	particles hierarchical ZSM-5	80%	[10]
6	*n*-octane	500 ℃ TOS = 120 s	monolith ($^1RC_{ZSM\text{-}5}$ = 41.2%)	54.3%	this work
7	*n*-octane	530 ℃ TOS = 170 min	particles [Al, Mg]-ZSM-5	97%	[11]
8	*n*-octane	600 ℃ TOS = 10 h	particles phosphorus-modified ZSM-5	90%	[12]
9	*n*-octane	550 ℃ TOS = 170 min	particles mesoporous ZSM-5	95%	[13]
10	*n*-octane	650 ℃ WHSV = 2.8 h^{-1}	particles nanosheet-stacked hierarchical ZSM-5	99%	[14]

4 Supplementary Figures

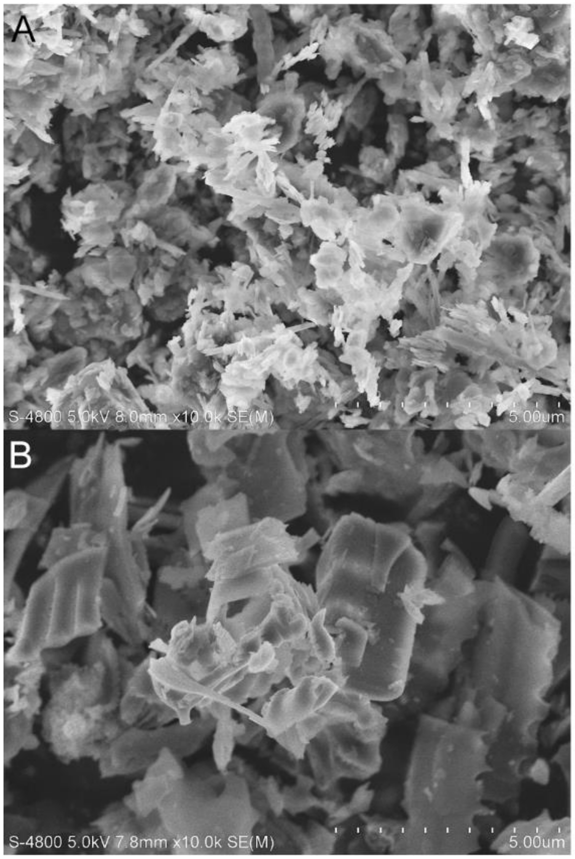

Figure S1. SEM images of (A) metakaolin and (B) diatomite.

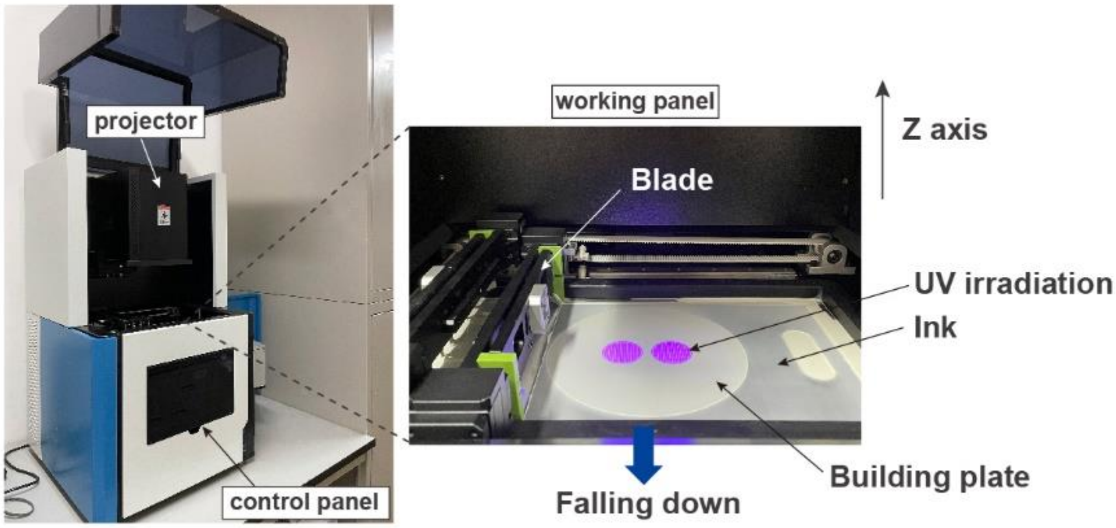

Figure S2. Digital photograph of the DLP 3D printer used in this work.

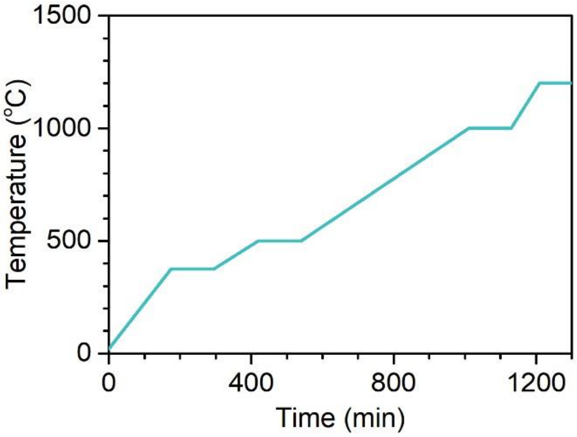

Figure S3. Heating program of the debinding process of the printed green body.

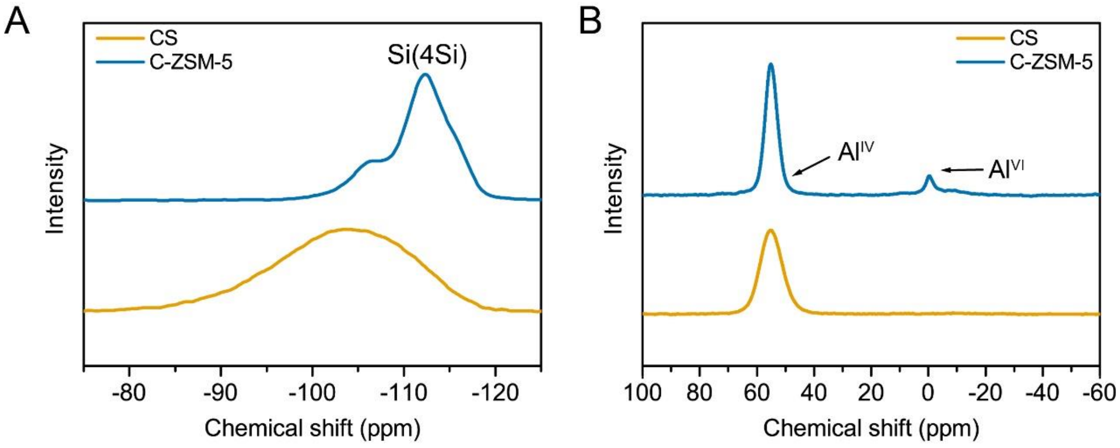

Figure S4. (A) ^{29}Si and (B) ^{27}Al MAS NMR of crystal seed (CS) and C-ZSM-5.

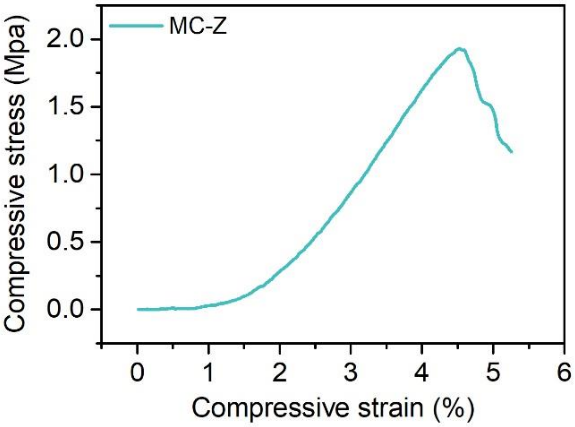

Figure S5. Compressive stress-strain curve for MC-Z.

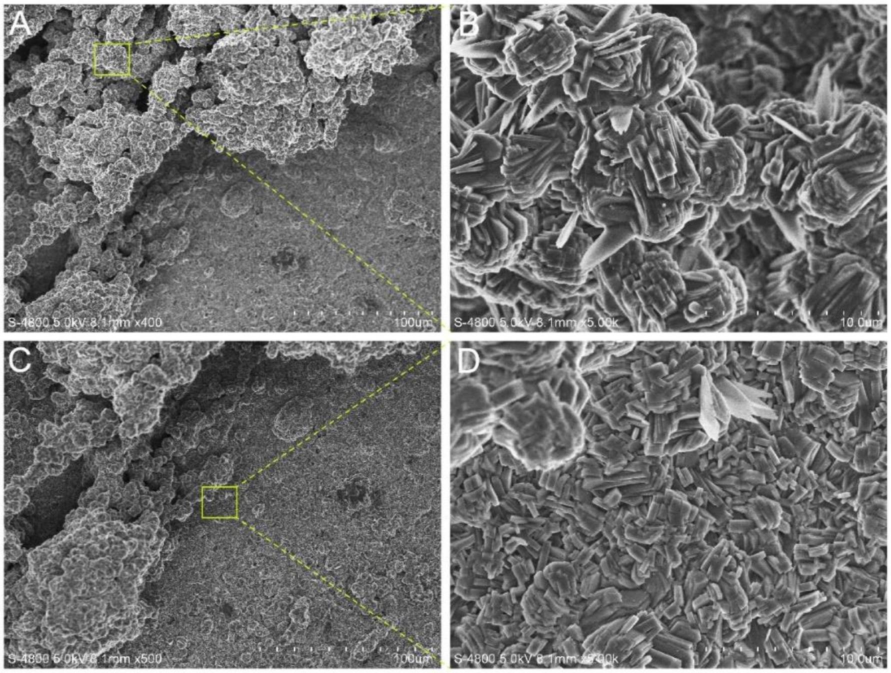

Figure S6. Morphologies and microstructures of the monolith catalyst (MC-Z). SEM image of the protrusions emerged on the surface of MC-Z at (A) low and (B) high magnifications. SEM image of the flat region observed on the surface of MC-Z at (C) low and (D) high magnifications.

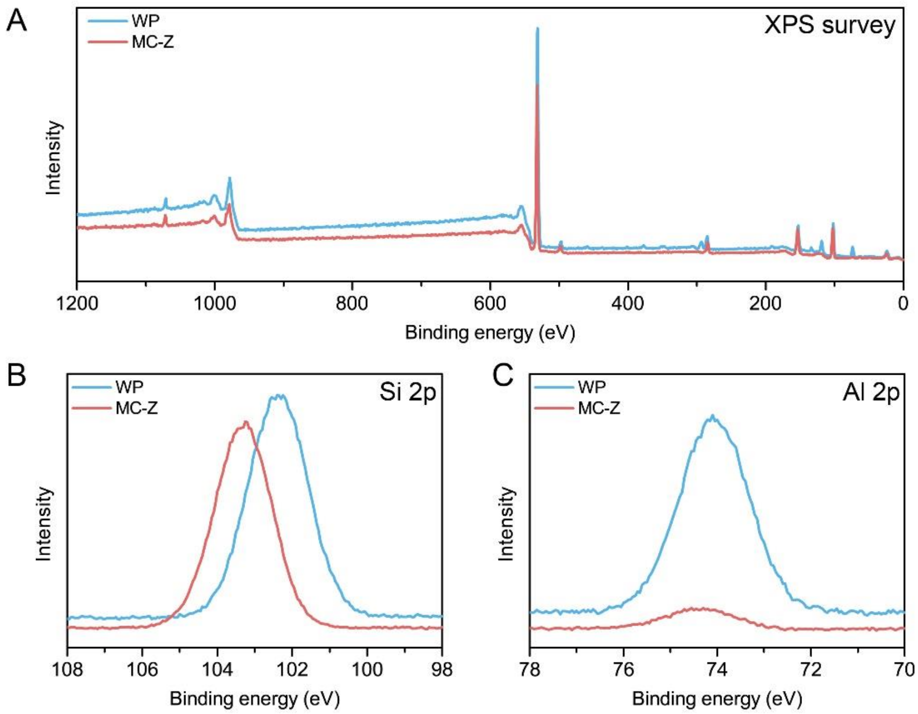

Figure S7. XPS spectra of the monolith catalyst (MC-Z) and the WP scaffold.

(A) XPS survey. (B) Si 2p spectra. (C) Al 2p spectra.

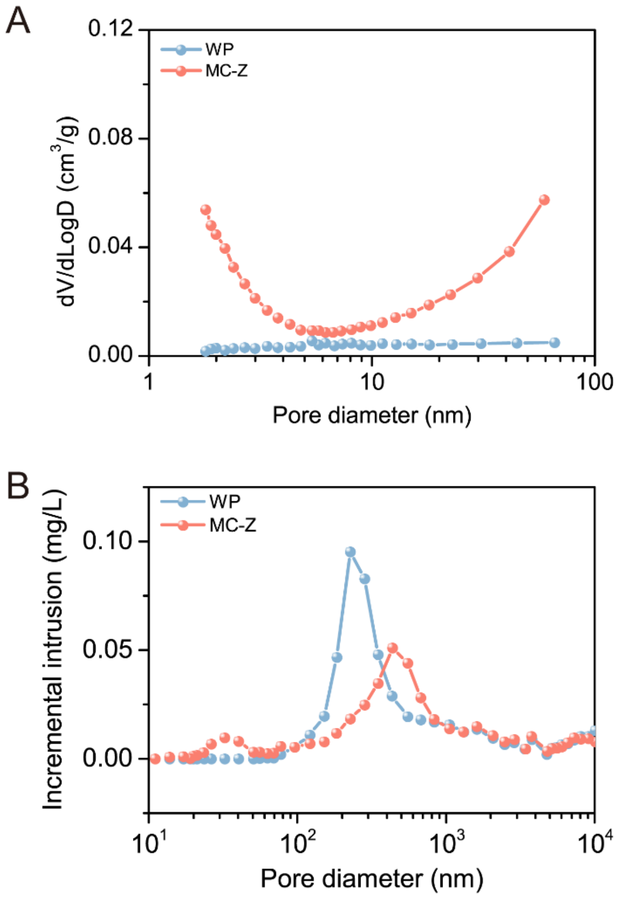

Figure S8. Pore size distribution profiles of WP scaffold and MC-Z.

(A) Barret–Joyner–Halenda (BJH) profiles derived from the adsorption branch.

(B) Mercury intrusion porosimetry profiles.

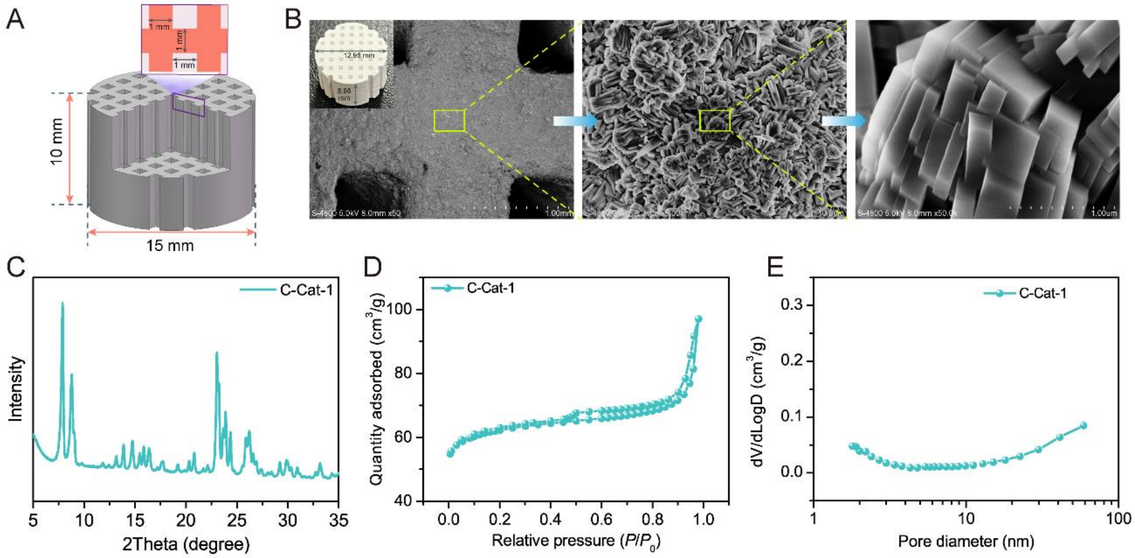

Figure S9. Properties of the control catalyst (C-Cat-1).

(A) Sectional view and geometric information of the three-dimensional model corresponding to straight-channelled C-Cat-1. (B) SEM images of the straight-channelled monolith catalyst bearing *in-situ* crystallized ZSM-5 zeolites (C-Cat-1). Inset: digital photograph of C-Cat-1. (C) XRD pattern. (D) N_2 adsorption-desorption isotherm. (E) Barret–Joyner–Halenda (BJH) pore size distribution profile derived from the adsorption branch.

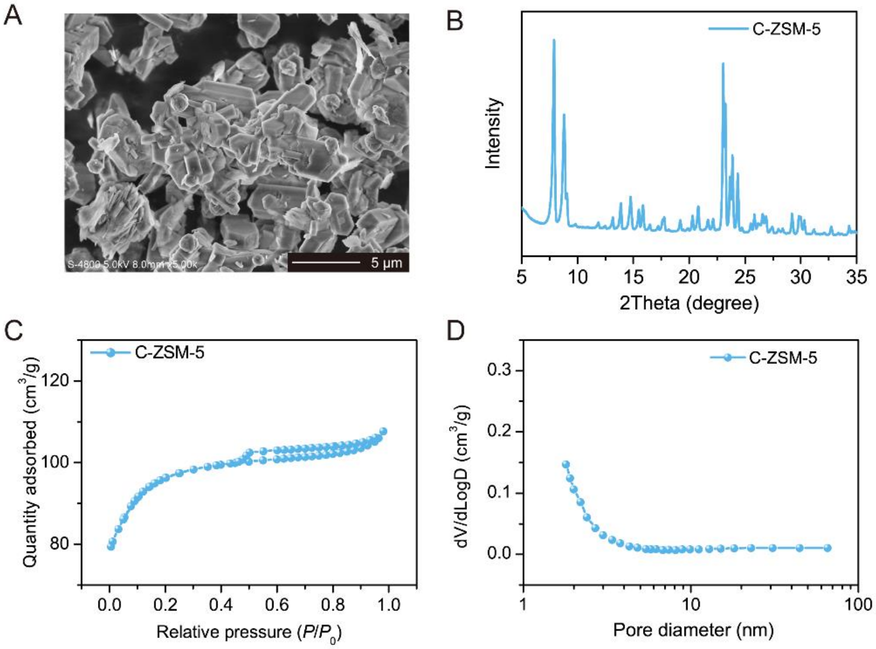

Figure S10. Properties of the commercial zeolite (C-ZSM-5) in C-Cat-2.

(A) SEM image. (B) XRD pattern. (C) N_2 adsorption-desorption isotherm. (D) Barret–Joyner–Halenda (BJH) pore size distribution profile derived from the adsorption branch.

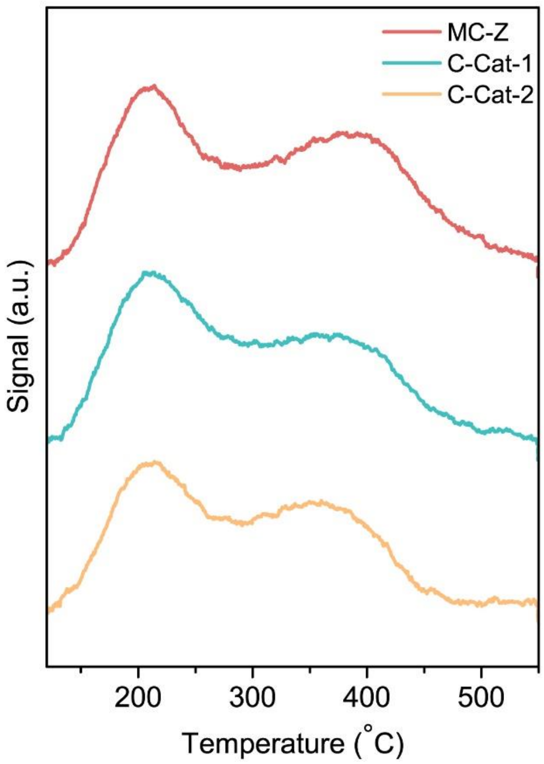

Figure S11. NH_3-TPD curves of different catalysts used in this work.

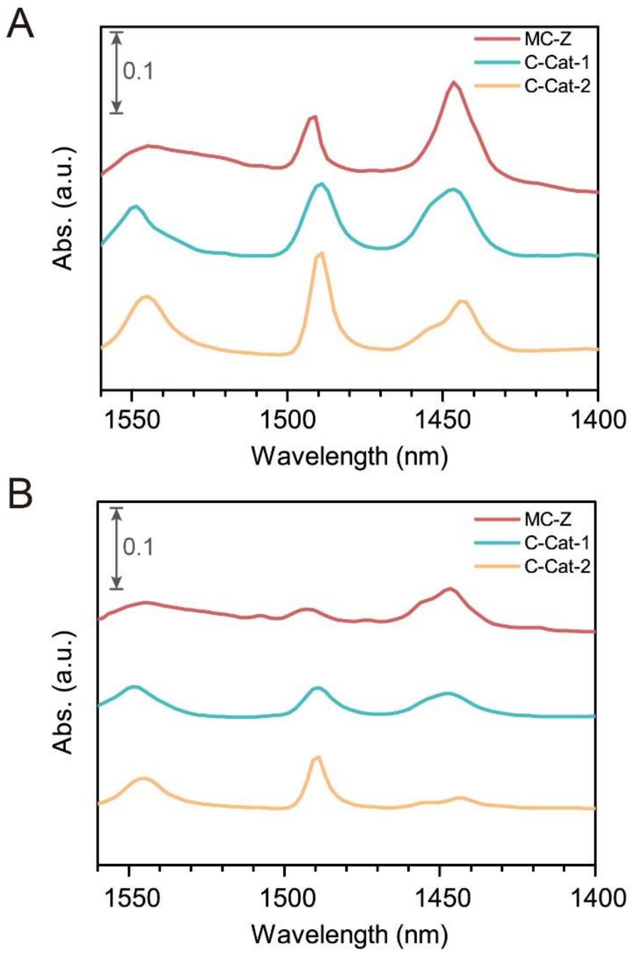

Figure S12. FTIR spectra of pyridine adsorbed on different catalysts.

(A) 200 ºC and (B) 350 ºC.

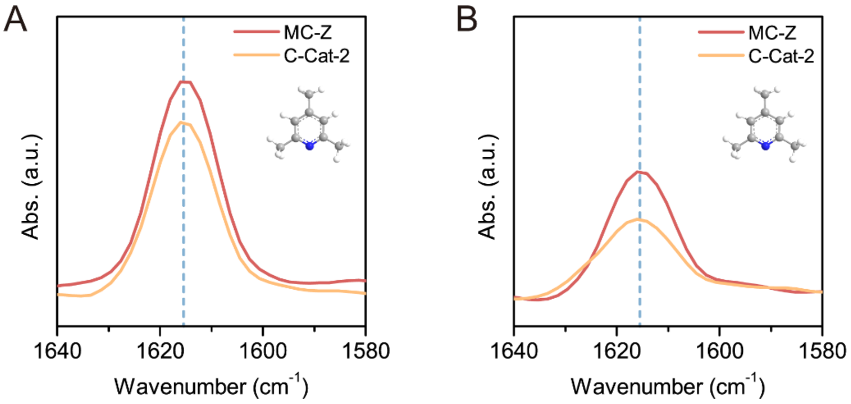

Figure S13. FTIR spectra of 2,4,6-collidine adsorbed on different catalysts. (A) 200 ºC and (B) 350 ºC.

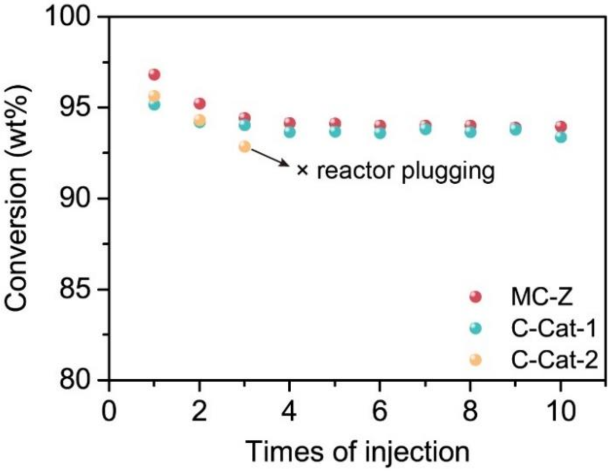

Figure S14. Deactivation behaviors of three catalysts in the cracking of TIPB under harsh conditions (650 ºC).

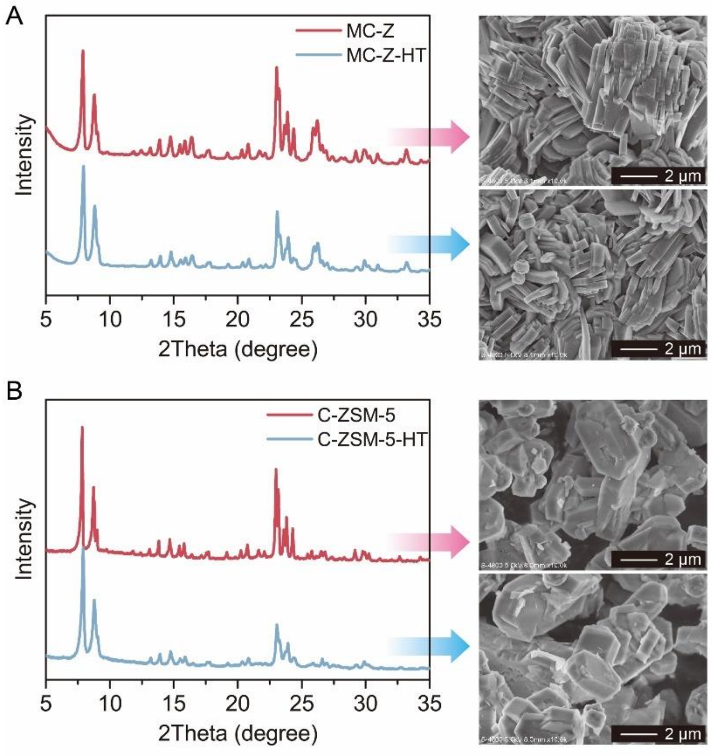

Figure S15. XRD patterns and SEM images of **(A)** MC-Z and **(B)** C-ZSM-5 before and after the hydrothermal treatment (800 ºC, 17 h).

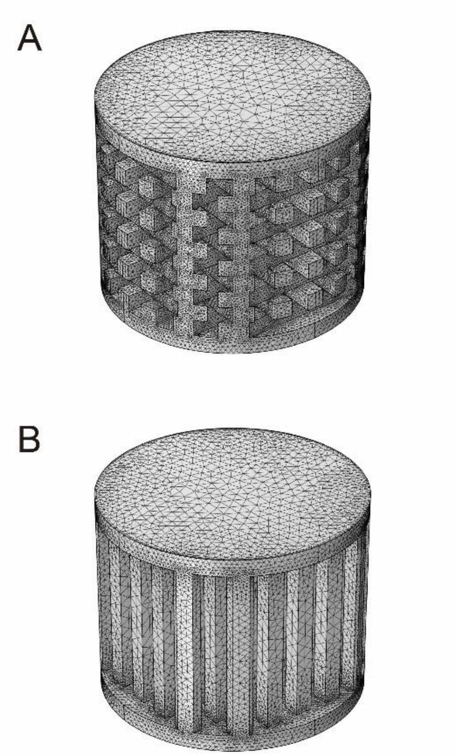

Figure S16. Fluid domain mesh for CFD analysis.

(A) Woodpile structured MC-Z. (B) Straight-channelled C-Cat-1.

5 References in supplementary material

1. NIST Standard Reference Database 4, 1999.
2. X. Li, W. Li, F. Rezaei and A. Rownaghi, *Chemical Engineering Journal*, 2018, **333**, 545-553.
3. E. Hędrzak, A. Węgrzynowicz, R. Rachwalik, B. Sulikowski and P. Michorczyk, *Applied Catalysis A: General*, 2019, **579**, 75-85.
4. C. Y. Chaparro-Garnica, P. Jordá-Faus, E. Bailón-García, R. Ocampo-Pérez, C. G. Aguilar-Madera, A. Davó-Quiñonero, D. Lozano-Castelló and A. Bueno-López, *ACS Applied Materials & Interfaces*, 2020, **12**, 54573-54584.
5. A. Lind, Ø. Vistad, M. F. Sunding, K. A. Andreassen, J. H. Cavka and C. A. Grande, *Materials & Design*, 2020, **187**, 108377.
6. X. Li, A.-A. Alwakwak, F. Rezaei and A. A. Rownaghi, *ACS Applied Energy Materials*, 2018, **1**, 2740-2748.
7. X. Dong, S. Shaikh, J. R. Vittenet, J. Wang, Z. Liu, K. D. Bhatte, O. Ali, W. Xu, I. Osorio, Y. Saih, J.-M. Basset, S. A. Ali and Y. Han, *ACS Sustainable Chemistry & Engineering*, 2018, **6**, 15832-15840.
8. W. Dai, L. Zhang, R. Liu, G. Wu, N. Guan and L. Li, *ACS Applied Materials & Interfaces*, 2022, **14**, 11415-11424.
9. X. Yang, X. Ma, X. Wang, B. Qin, L. Zhang, Y. Du, Y. Liu, Q. Wang, Y. Wang and J. Zheng, *Journal of Porous Materials*, 2023, DOI: 10.1007/s10934-023-01444-0.
10. Q. Wang, L. Zhang, Z. Yao, Y. Guo, Z. Gao, J. Zheng, W. Li, B. Fan, Y. Wang, S. Chen and R. Li, *Materials Chemistry and Physics*, 2020, **243**, 122610.
11. K. Chen, X. Wu, J. Zhao, H. Zhao, A. Li, Q. Zhang, T. Xia, P. Liu, B. Meng, W. Song, X. Zhu, H. Liu, X. Gao, C. Xu and B. Shen, *Journal of Catalysis*, 2022, **413**, 735-750.
12. P. Wattanapaphawong, P. Reubroycharoen, N. Mimura, O. Sato and A. Yamaguchi, *Fuel Processing Technology*, 2020, **202**, 106367.
13. X. Xiao, B. Sun, P. Wang, X. Fan, L. Kong, Z. Xie, B. Liu and Z. Zhao, *Microporous and Mesoporous Materials*, 2022, **330**, 111621.
14. P. Wang, X. Xiao, Y. Pan, Z. Zhao, G. Jiang, Z. Zhang, F. Meng, Y. Li, X. Fan, L. Kong and Z. Xie, *Catalysts*, 2022, **12**, 351.